Eu^{3+}- activated Sr$_2$GdF$_7$ colloid and nano-powder for horticulture LED applications

Bojana Milićević [a,*], Aleksandar Ćirić [a], Zoran Ristić [a], Mina Medić [a], Abdullah N. Alodhayb [b], Ivana Radosavljević Evans [c], Željka Antić [a], Miroslav D. Dramićanin [a,*]

[a] Centre of Excellence for Photoconversion, Vinča Institute of Nuclear Sciences - National Institute of the Republic of Serbia, University of Belgrade, Belgrade, Serbia
[b] King Abdullah Institute for Nanotechnology, King Saud University, Riyadh 11451, Saudi Arabia
[c] Department of Chemistry, Durham University, Durham DH1 3LE, UK

ARTICLE INFO

ABSTRACT

A series of multifunctional Sr$_2$Gd$_{1-x}$Eu$_x$F$_7$ ($x = 0$, 0.05, 0.10, 0.40, 0.60. 0.80, and 1.00) phosphors in stable colloidal form and as nanopowders have been prepared using a hydrothermal method. Powder X-ray diffraction analysis confirmed that the materials crystallize in a cubic crystal structure. Transmission electron microscopy shows quasi-spherical nanoparticles with an average particle size of ~24 nm. Photoluminescence measurements show highly efficient red emission in both colloids and nanopowders, with intensity continually increasing up to 80 mol% of Eu^{3+} content without concentration quenching. The most prominent emission peaks are around 600 nm (orange/red) and 700 nm (deep red), with the latter more pronounced. Quantum efficiency follows a similar trend, and reaches 60 % for the sample with 80 mol% of Eu^{3+} content. In addition, similar asymmetry ratio values and CIE coordinates show that there is not a big change in the local symmetry around Eu^{3+} ions or emission color across the series. This confirms that Eu^{3+} resides in the same crystalline environment in samples. The observed ^{5}D$_0$-level lifetimes gradually decrease from 12.0 ms to 6.9 ms as the Eu^{3+} concentration increases. Judd-Ofelt parameters show slight variation with Eu^{3+} concentration with Ω_4 always larger than Ω_2. The temperature-dependent steady-state and time-resolved photoluminescence measurements demonstrate high stability of nanopowders' emission up to 100 °C. The combination of temperature stability and high efficiency of emission, as well as the untypical dominant deep-red emission at 700 nm labels these nanoparticles as potential nanophosphors for various applications.

1. Introduction

Lanthanide-based luminescent materials emit electromagnetic radiation over the ultraviolet, visible, and infrared spectral regions and can be polyvalent building blocks for innovative technologies with the potential to address different societal challenges. Typically, they exhibit exceptional optical properties, such as narrow emission bands and long emission decay times. These properties are relevant to applications in biotechnology, medicine, optoelectronics, energy harvesting and conversion, data storage, fast and secure telecommunication, and security. Numerous studies have demonstrated a variety of materials with various compositions and morphologies to meet the demands of real-life applications [1–9].

Trivalent lanthanide ion-doped nanoparticles serve as a class of luminescent nanomaterials, offering a convenient platform for regulating optical emission through downshifting, downconversion, and upconversion mechanisms. The abundance of emitting levels at different energies, among other unique attributes, has generated considerable research interest for lanthanide nanoparticles in science and technology. Different applications require different properties. For example, in the field of nanotechnology for applications such as bioimaging and diagnostic probes, novel optical probes, and therapeutic agents, intense research is ongoing to develop new advanced optical nanomaterials [10–13]. To be used in living organisms, these materials ought to be in colloidal form, functionalized for selective targeting, and have the ability to tune optical properties to luminescence inside biological transparency windows. In agriculture, an efficient plant-growth-targeted light-emitting diode (LED) must convert as much electrical energy as possible into Photosynthetically Active Radiation (PAR) region, the spectral range of solar radiation from 400 to 700 nm

that organisms can use in the process of photosynthesis. In addition, it was recently demonstrated that deep-red photons (700—750 nm) interact with higher-energy photons to increase plant photochemical efficiency [14], resulting in improved flavor quality and reduced bitterness caused by excessive leafy plant growth (e.g., lettuce, spinach). Horticulture-specific luminaires are designed to decrease energy consumption, which is crucial in the face of rising energy costs and energy-saving limitations. In this sense, the LED output that matches the PAR spectrum with additional deep-red components is needed for the future of agriculture production. Red and far-red light matches the absorption spectra of phytochrome plant photoreceptors, including P_R (550—700 nm) and P_{FR} (600—800 nm), respectively. Adjusting the ratio of these two photoreceptors can control the specific germination of seeds or the expansion of leaves, influencing plant morphogenesis throughout their lives. For that, developing red and far-red emitting phosphors with excitation spectra that match well with the emission bands of commercial LED chips; emission spectra that match absorption of both P_R and P_{FR} photoreceptors, highly efficient and thermally stable (up to the operating temperature of LEDs) phosphors for horticulture LEDs is crucial [7,15].

Here, we intend to create a phosphor that provides both strong red and deep-red emissions that can be suitable for developing horticulture LEDs. We synthesized Eu^{3+}-doped Sr_2GdF_7 (SGF) nanophosphors in both colloid and powder form using a low-temperature hydrothermal method for this purpose. We investigate in detail the structure, morphology, and photoluminescent properties of the $Sr_2GdF_7:Eu^{3+}$ colloids and nanopowders with various doping concentrations. The Judd-Ofelt analysis provided insight into the radiative properties of the material. The quantum efficiency measurements estimated emission efficiency. The temperature-dependent steady-state and time-resolved photoluminescence measurements demonstrated the good temperature stability of nanopowders' emissions. Finally, to exhibit the application potential of this system, an LED device was fabricated from $Sr_2Gd_{0.2}Eu_{0.8}F_7$ powder mixed with a ceramic binder and placed on top of a 365 nm near-UV chip.

2. Experimental

2.1. Synthesis of colloidal Eu^{3+}-doped Sr_2GdF_7 nanoparticles

Strontium nitrate ($Sr(NO_3)_2$, Alfa Aesar Karlsruhe, Germany, 99 %), gadolinium (III) nitrate hexahydrate ($Gd(NO_3)_3 \cdot 6H_2O$, Alfa Aesar, Karlsruhe, Germany, 99.9 %), europium (III) nitrate hexahydrate, ($Eu(NO_3)_3 \cdot 6H_2O$, Alfa Aesar, Karlsruhe, Germany, 99.9 %), disodium ethylenediaminetetraacetate dihydrate (EDTA-2Na, $C_{10}H_{14}N_2O_8Na_2 \cdot 2H_2O$, Kemika, Zagreb, Croatia, 99 %),), ammonium fluoride (NH_4F, Alfa Aesar, Karlsruhe, Germany, 98 %), 25 % ammonium solution (NH_4OH, Fisher, Loughborough, Leicestershire, United Kingdom) and deionized water were used as starting materials without further purification.

The hydrothermal method was used to prepare a set of seven $Sr_2Gd_{1-x}Eu_xF_7$ ($x = 0$, 0.05, 0.10, 0.40, 0.60. 0.80, and 1.00, where mol.% of Eu^{3+} dopant ions were added with respect to Gd^{3+}) colloids, as illustrated in Fig. 1. A typical synthesis procedure includes metal nitrates and NH_4F as precursors and EDTA-2Na as a stabilizing agent [16]. Due to the ability to improve crystalline seed dispersibility by forming $[Sr-EDTA]^{2+}$ and $[Gd-EDTA]^+$ complexes after mixing all the chemicals, EDTA-2Na prevented SGF particle aggregation during the subsequent hydrothermal treatment. At the same time, $[Gd-EDTA]^+$ cations are adsorbed on the surfaces of SGF particles, additionally improving their stability. Typically, for the synthesis, all nitrates were weighed according to the stoichiometric ratio and dissolved in 12.5 ml of deionized water while stirring at room temperature. The solutions were mixed for 30 min with a transparent solution of EDTA-2Na in 12.5 ml of water (molar ratio EDTA-2Na:Ln = 1:1). Following that, 10 ml of NH_4F aqueous solution (molar ratio NH_4F:Ln = 12:1) was added and vigorously stirred for 1 h, yielding a white suspension. The pH value of the mixture was adjusted to around 6 using NH_4OH. Hydrothermal treatment was carried out in a 100-ml Teflon-lined autoclave in the oven at 180 °C for 20 h followed by natural cooling. Obtained colloidal suspensions were acidic with pH = 6. The described method produced undoped SGF and SGF phosphors with varying concentrations of Eu^{3+} ions. The colloidal suspensions were dried in the air, and obtained powders used for XRD analysis, diffuse reflectance, and temperature-dependent photoluminescent measurements. The amounts of precursors used for synthesizing ~0.0025 mol
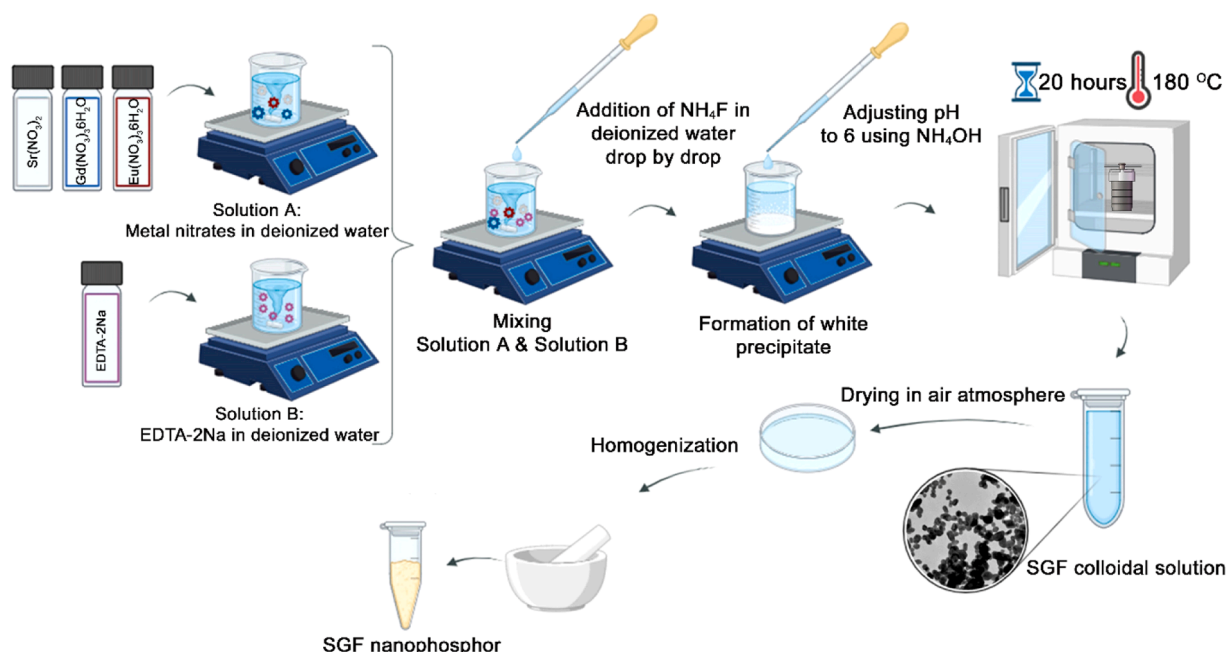

Fig. 1. Schematic illustration of the colloidal and powder SGF:Eu nanophosphors preparation.

(~1.2 g) of samples are given in Table 1.

2.2. Characterization

The phase identity and crystal structure of the samples were investigated by PXRD using the Rigaku SmartLab instrument (Cu-Kα1,2 radiation; λ = 1.54 Å) at room temperature. Data were recorded over the 6°—130° 2θ range, with a step size of 0.01° and a counting time of 1°/min. PXRD data were analyzed by the Rietveld method implemented in TOPAS Academic software [17,18]. The refined parameters included a unit cell parameter, an overall isotropic atomic displacement parameter, scale factor, sample height displacement, pseudo-Voigt peak shape function terms, and background polynomial terms. The microstructure was investigated by TEM JEOL JEM1011 operated at an accelerating voltage of 100 kV. The average particle size was calculated using ImageJ software. Diffuse reflectance measurements were performed with the Shimadzu UV-2600 (Shimadzu Corporation, Tokyo, Japan) spectrophotometer equipped with an integrating sphere (ISR-2600), using BaSO₄ as the standard reference. Photoluminescence measurements were carried out using a Fluorolog-3 Model FL3–221 spectrofluorometer system (Horiba Jobin-Yvon) equipped with R928 PMT. Emission and excitation spectra were corrected for the lamp spectral intensity and detector sensitivity. Excited-state lifetime measurements were carried out using the Rohde&Schwarz RTC1002 two-channel oscilloscope paired with the Hamamatsu H10722–20 photomultiplier tube, and by exciting the samples with a square wave modulated Ocean Insight fiber-coupled LED (LSM-405A LED Light Source) controlled by Ocean Insight LDC-1 Single Channel LED Controller. Quantum efficiency measurements were performed using a home-built system, consisting of Ocean Insight IDP-REF 38.1 mm integrating sphere fiber coupled to the Ocean Insight LSM-405A LED light source on the reference port and the OCEAN-FX-XR1-ES extended range spectrometer on the sample port of the sphere, using BaSO₄ as the standard reference. CIE coordinates were calculated using the Color Calculator by OSRAM Sylvania, Inc. Temperature-dependent photoluminescence measurements were performed using the MicroOptik heating stage.

3. Results and discussion

3.1. Structure, morphology, and diffuse reflectance

Powder X-ray diffraction (PXRD) patterns of $Sr_2Gd_{1-x}Eu_xF_7$ (x = 0, 0.05, 0.10, 0.40, 0.60. 0.80, and 1.00) nanophosphors are shown in Fig. 2a, with Rietveld refinement fits for the two end members, Sr_2GdF_7 (SGF) and Sr_2EuF_7 (SEF), given as Fig. 2b-c (R_{wp} = 2.72 % and 3.43 %, respectively). The patterns of Sr_2GdF_7 and Sr_2EuF_7 were fitted using a structural model in the cubic space group $Fm\bar{3}m$ (225), with Sr and Gd ions on Wyckoff site 4a with m-3m symmetry and F ions on Wyckoff site 8c with −43 m symmetry. While in the ideal fluorite-type compound of MX_2 stoichiometry the cations are found in 8-coordinate cubic environments and the anions in 4-coordinate tetrahedral environments, the partial occupancies of both cation and anion sites in Sr_2GdF_7 and Sr_2EuF_7 result in deviations from these ideal coordination geometries

and a range of environments is expected to exist for the species present. The obtained unit cell parameters were 5.7484(1) Å for SGF and 5.7618 (1) Å for SEF. All observed reflections were accounted for in PXRD patterns of all samples, and the absence of extra peaks confirms the phase purity of the materials prepared. Due to smaller ionic radii of Gd^{3+} (Gd^{3+}_{VIII} = 1.053 Å, [19]) incorporation of larger Eu^{3+} (Eu^{3+}_{VIII} = 1.066 Å, [19]) ions resulted in shifting of diffraction peaks to lower Bragg angles, consistent with the unit cell parameters obtained for the two end members (see Fig. 2d).

There appears to be some misunderstanding in the literature about the crystal structure adopted by Sr_2GdF_7 and related compounds, with some articles reporting cubic $Fm\bar{3}m$ structure and others a tetragonal structure with unit cell parameters a = 4.06 Å, c = 11.54 Å [20–28]. It is worth noting, however, that a number of articles that state that the structure of Sr_2GdF_7 is tetragonal show PXRD data without any tetragonal superstructure peaks observed and the patterns given are consistent with a cubic structure, as is the case with the materials produced and characterized in this work. It is conceivable that prolonged annealing of these hydrothermally prepared samples at high temperatures would result in the transformation of the disordered cubic fluorite-type structure into an ordered tetragonal superstructure. Accurate and detailed insight into the evolution of structure on different length-scales in these cases can be obtained using local structure investigation methods such as total scattering and reverse Monte Carlo modelling [29].

Transmission electron microscopy (TEM) images of representative colloidal SGF_40 %Eu³⁺ particles, obtained with different magnifications, are shown in Fig. 2e-f. Nanoparticles show a similar quasi-spherical shape with the average particle size estimated to be 24 ± 2 nm (see the histogram fitted with a log-normal distribution, based on around 200 particles, Fig. 2e inset).
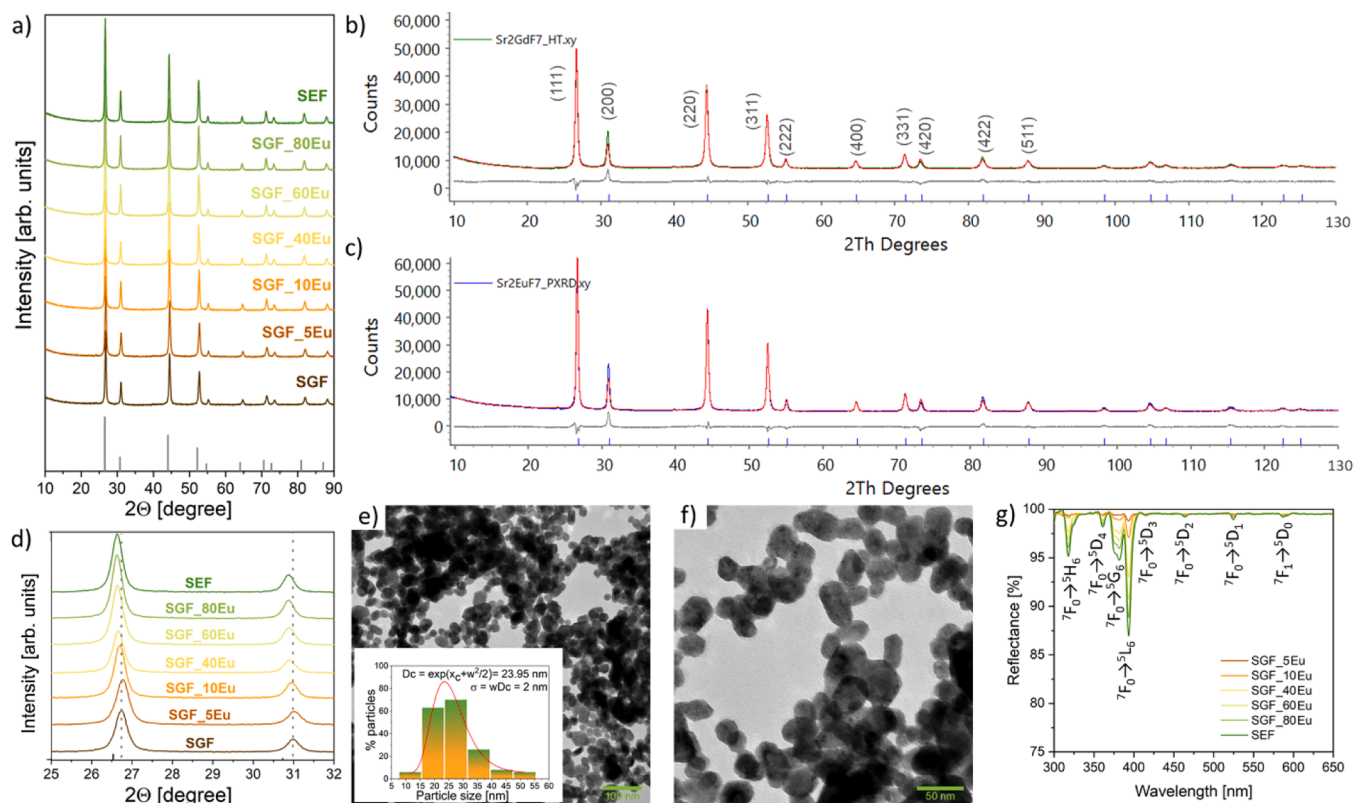
Fig. 2g shows the room temperature diffuse reflectance spectra of $Sr_2Gd_{1-x}Eu_xF_7$ (x = 0, 0.05, 0.10, 0.40, 0.60. 0.80, and 1.00) samples in the 300–650 nm wavelength range, which display typical optical features of Eu^{3+} ions [30]. The absorption peaks of Eu^{3+} ions, which are located at 317, 360, 381, 394, 414, 464, 525, and 587 nm correspond to the following electronic transitions: $^7F_0 \rightarrow {}^5H_3$, $^7F_0 \rightarrow {}^5D_4$, $^7F_0 \rightarrow {}^5G_6$, $^7F_0 \rightarrow {}^5L_6$, $^7F_0 \rightarrow {}^5D_3$, $^7F_0 \rightarrow {}^5D_2$, $^7F_0 \rightarrow {}^5D_1$, and $^7F_1 \rightarrow {}^5D_0$, respectively, with the highest absorption at around 394 nm.

3.2. Photoluminescent properties

It is generally acknowledged that the energy levels of a rare-earth ion are split in the crystal field produced by the host and this splitting depends on the crystal structure of the host. The Eu^{3+} ion has the [Xe]4f^6 electronic configuration and when it is situated on a centrosymmetric site, according to the Laporte rule, only magnetic-dipole transitions are possible. On the other hand, if Eu^{3+} ion occupies a non-centrosymmetric site both magnetic-dipole and electric-dipole transitions are possible.

The room temperature photoluminescence excitation spectra of all $Sr_2Gd_{1-x}Eu_xF_7$ colloids recorded in the 250–330 nm ($λ_{em}$ = 698 nm) and 310—570 nm ($λ_{em}$ = 593 nm) ranges are given in Fig. 3a-b, showing lines that correspond to transitions within the 4f^6 configuration of Eu^{3+} and 4f^7 configuration of Gd^{3+}. Excitations centered around 273 and 311 nm correspond to Gd^{3+} absorption. The intensity of Gd^{3+} peaks is the largest for the $Sr_2Gd_{0.9}Eu_{0.1}F_7$ composition (90 mol% of Gd^{3+} and 10 mol% of Eu^{3+}), indicating the optimal Eu/Gd ratio for energy transfer from Gd^{3+} to Eu^{3+}.

Photoluminescence emission spectra of all $Sr_2Gd_{1-x}Eu_xF_7$ colloids recorded at room temperature are given in Fig. 3c ($λ_{ex}$ = 273 nm) and Fig. 3d ($λ_{ex}$ = 394 nm). Emission centered at 311 nm, presented in Fig. 3c, corresponds to the $^6P_J \rightarrow {}^8S_{7/2}$ transition of Gd^{3+}, while those at longer wavelengths correspond to 4f—4f transitions of Eu^{3+} (Fig. 3d) placed at ~592 nm ($^5D_0 \rightarrow {}^7F_1$), ~613 nm ($^5D_0 \rightarrow {}^7F_2$), ~650 nm ($^5D_0 \rightarrow {}^7F_3$), and ~700 nm ($^5D_0 \rightarrow {}^7F_4$). If the excitation is in Gd^{3+} ion, either Gd^{3+} radiates with 310 nm emission or it transfers energy to the Eu^{3+}.

Table 1
The amounts of precursors needed for synthesizing 0.0025 mol of samples.

	Sr (NO₃)₂ (g)	Gd (NO₃)₃·6H₂O (g)	Eu (NO₃)₃·6H₂O (g)	NH₄F** (g)	EDTA (g)
SGF	1.0582	1.1284	—	1.1111	0.9306
SGF_5Eu	1.0582	1.0720	0.0557	1.1111	0.9306
SGF_10Eu	1.0582	1.0156	0.1115	1.1111	0.9306
SGF_40Eu	1.0582	0.6770	0.4460	1.1111	0.9306
SGF_60Eu	1.0582	0.4514	0.6690	1.1111	0.9306
SGF_80Eu	1.0582	0.2257	0.8919	1.1111	0.9306
SEF	1.0582	—	0.9306	1.1111	0.9306

Fig. 2. (a) XRD patterns of $Sr_2Gd_{1-x}Eu_xF_7$ ($x = 0.05, 0.10, 0.40, 0.60. 0.80$, and 1.00) nanophosphors; (b, c) Rietveld fits for Sr_2GdF_7 and Sr_2EuF_7. Green (SGF) and blue (SEF) curves represent the observed pattern, in each case, the red curves are the calculated patterns, and the difference curves are shown in grey, while blue tick marks represent the positions of the Bragg peaks; (d) Enlarged (111) and (200) diffraction peaks showing a shift toward lower Bragg angels due to the replacement of Gd with Eu ions in the host material; (e, f) TEM images under different magnification with the particle size distribution of representative colloidal SGF:40 mol% Eu^{3+} given as Inset in Fig. 2e; (g) Room temperature diffuse reflectance spectra for all $Sr_2Gd_{1-x}Eu_xF_7$ ($x = 0.05, 0.10, 0.40, 0.60. 0.80$, and 1.00) samples.

Then the Eu^{3+} ion de-excites to the lower excited levels from which it radiatively de-excites to the ground multiplet. Alternatively, the Eu^{3+} may absorb UV photons directly, most efficiently at 394 nm, and undergo the same de-excitation pathway as with the ET from the Gd^{3+} ion. These mechanisms are depicted in Fig. 3e. Emission peaks from $^5D_1$, $^5D_2$, and $^5D_3$ levels (Fig. 3d inset) are the most intense with 10 mol% of Eu^{3+} because of earlier concentration quenching of energetically higher Eu^{3+} levels [31].

The $^5D_0 \rightarrow ^7F_1$ is a magnetic-dipole transition that does not depend on the local environment. However, the $^5D_0 \rightarrow ^7F_2$ electric-dipole transition is a hypersensitive one, and it is highly dependent on changes in the local environment around the Eu^{3+} ions. Theoretically, when the Eu^{3+} ions occupy centrosymmetric sites, the emission spectrum shows a more intense $^5D_0 \rightarrow ^7F_1$ transition than the $^5D_0 \rightarrow ^7F_2$ one. This agrees with our experimental observations. In addition, the ratio of the integrated intensity of the $^5D_0 \rightarrow ^7F_2$ and $^5D_0 \rightarrow ^7F_1$ transitions, known as the asymmetry ratio, can be considered indicative of the reduction of symmetry of the coordination environment around the Eu^{3+} ion, and is given by Eq. (1):

$$R = \frac{I(^5D_0 \rightarrow ^7F_2)}{I(^5D_0 \rightarrow ^7F_1)}. \tag{1}$$

The asymmetry ratio values obtained from the emission spectra do not vary significantly as a function of Eu^{3+} concentration, as shown in Fig. 3f. Therefore, one may conclude that the degree of distortion of the local symmetry around Eu^{3+} is similar in the samples in the series produced. This is consistent with the samples being isostructural, as shown by PXRD and Rietveld analysis.

Emission in the deep-red spectral region around 700 nm, which corresponds to the $^5D_0 \rightarrow ^7F_4$ transition, exhibits high intensity, even

higher than emission from $^5D_0 \rightarrow ^7F_1$ and $^5D_0 \rightarrow ^7F_2$ transitions. This is not common for Eu^{3+} and it was previously reported for several fluoride hosts where the structural distortion from the octahedral symmetry to the non-centrosymmetric D_{4d} occurs [32,33], as the odd-rank components of the static forced electric dipole and ligand polarizability-dependent dynamic coupling mechanisms are high, especially in the highly polarizable chemical environment [34]. This observation in our spectra is consistent with a range of Eu^{3+} environments present and the breaking of the centrosymmetric m-3m symmetry of the average long-range crystallographic model at a local level, due to the partial site occupancies. Fig. 3g shows that photoluminescent intensity continually increases as the Eu^{3+} content increases from 5 mol% to 80 mol%, without concentration quenching. The Eu^{3+} deep-red emission ($^5D_0 \rightarrow ^7F_4$) in SGF:Eu phosphors has a full width at a half-maximum of around 10 nm and fits the absorption band of phytochrome photoreceptors, P_{FR}. Furthermore, the Eu^{3+} red emission bands ($^5D_0 \rightarrow ^7F_1$ and $^5D_0 \rightarrow ^7F_2$) matched the red-adsorbing phytochrome photoreceptors, P_R, indicating that SGF:Eu may be an effective nanophosphor for horticulture LED applications. To evaluate real application potential, the absolute photoluminescent quantum efficiency was measured at room temperature with an integrating sphere, and the results are shown in Fig. 3g. The efficiency increases with Eu^{3+}-dopant concentration starting from 7 % for the 5 mol% doped sample and reaching 60 % for the 80 % doped sample.

Fig. 3h displays the normalized photoluminescent lifetime decay curves of the $Sr_2Gd_{1-x}Eu_xF_7$ ($x = 0.05, 0.10, 0.40, 0.60. 0.80$, and 1.00) colloids recorded at room temperature. To obtain the value of the lifetime (τ), acquired data were fitted to a simple single exponential function:
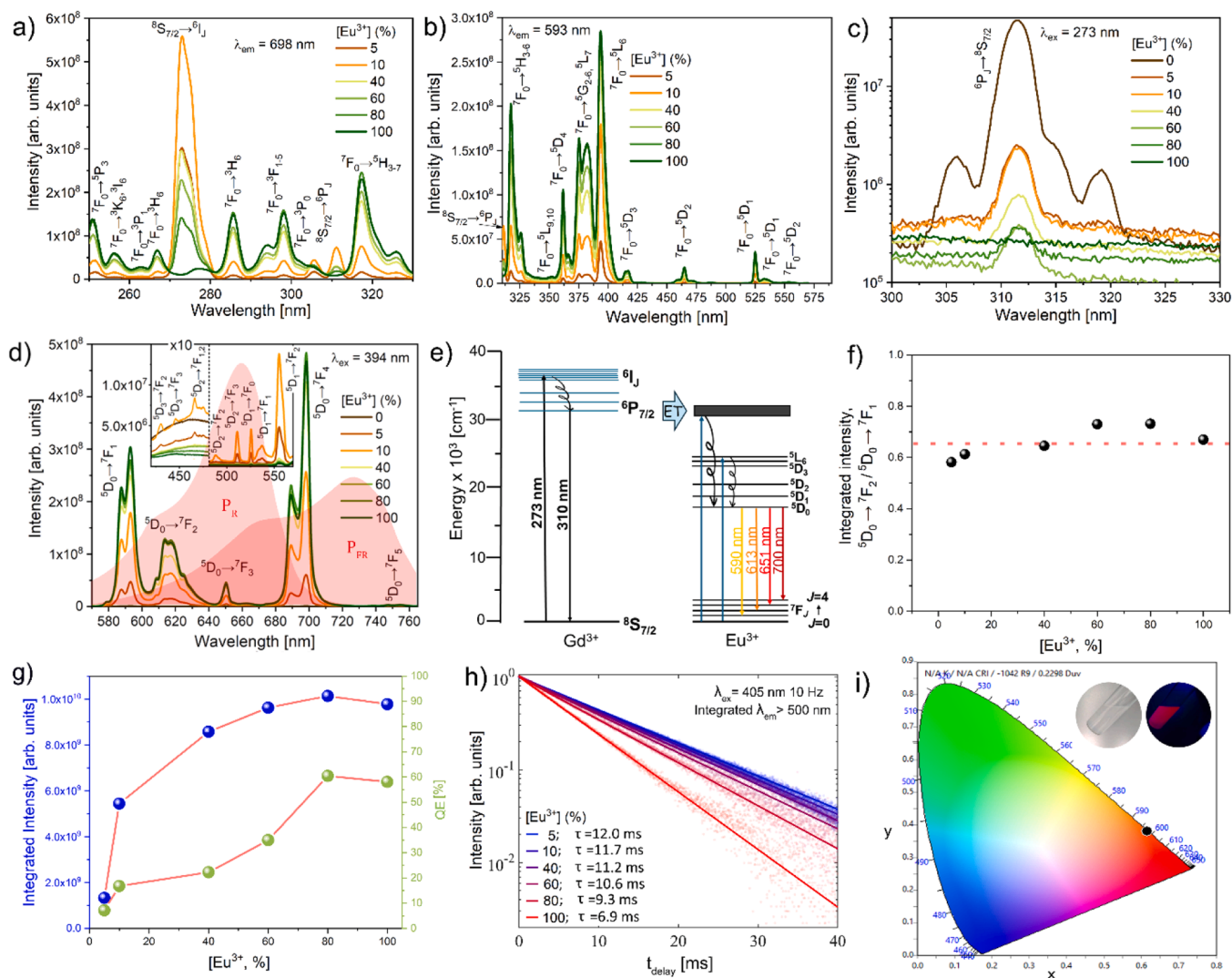
Fig. 3. Room temperature photoluminescence of $Sr_2Gd_{1-x}Eu_xF_7$ (x = 0.05, 0.10, 0.40, 0.60. 0.80, and 1.00) colloids: a) excitation spectra under λ_{em} = 698 nm; b) excitation spectra under λ_{em} = 593 nm; c) emission spectra under λ_{ex} = 273 nm; d) emission spectra under λ_{ex} = 394 nm (red pattern is the absorption spectra of P_R and P_{FR} photoreceptors); e) energy level diagram and energy transfer mechanism of Gd^{3+} and Eu^{3+} in SGF; f) asymmetry ratio as a function of Eu ions concentration; g) integrated emission intensity as a function of Eu ions concentration (blue dots) and quantum efficiency as a function of Eu ions concentration (green dots); h) lifetime decay curves as a function of Eu ions concentration; and i) CIE diagram with calculated coordinates of SGF_80Eu (Inset: appearance of colloid under daylight and near UV light).

$$I(t) = I_0 e^{-\frac{t}{\tau}}, \qquad (2)$$

where $I(t)$ represents the corresponding emission intensity at time t, I_0 represents the initial emission intensity (I_0 = 1 in normalized curves in Fig. 3h), and τ represents the emission decay constant (excited state lifetime). As the Eu^{3+} concentration increased, the $^5D_0$-level lifetimes gradually decreased from 12.0 to 6.9 ms. The shortening of the lifetime with increasing concentration indicates the activation of concentration-quenching mechanisms. These quenching mechanisms compete with the increase in emission intensity due to an increase in the number of optically active centers when Eu^{3+} concentration is increased, resulting in an intensity net rise with concentrations up to 80 % of Eu^{3+} content.

Chromaticity coordinates (x,y) on the CIE chromaticity diagram, a two-dimensional color space that describes all the colors observed by the human eye, can be used to quantify apparent color. We derived the CIE chromaticity coordinates from the photoluminescent spectra to evaluate the color of the synthesized samples, as shown in Fig. 3i and Table 2. For all the samples, CIE coordinates are almost identical for the highly doped samples (x = 0.62, y = 0.38; λ_{dom} = 598 nm; color purity = 99.1 %) and placed in the orange-red portion of the diagram, confirming that there is no significant change in the local symmetry around Eu^{3+} across the series and consequently in the emission spectra. Inset in Fig. 3i shows the translucent white color of colloids under daylight and the red appearance of colloids under UV light.

Table 2
Chromaticity coordinates (x,y) of SGF:Eu.

	SGF_5Eu	SGF_10Eu	SGF_40Eu	SGF_60Eu	SGF_80Eu	SEF
CIE (x, y) coordinates	(0.565,0.398)	(0.586,0.396)	(0.611,0.384)	(0.615,0.381)	(0.616,0.381)	(0.614,0.383)

3.2.1. Judd-Ofelt analysis

The quantum mechanical, semi-empirical, Judd-Ofelt theory [35, 36], introduced in the 1960s, presents a centerpiece in lanthanide spectroscopy [37], as the only theory that can explain and predict radiative properties of intra-configurational luminescence in ions from Pr^{3+} to Tm^{3+}. From only three intensity parameters, the theory provides an estimate of the radiative transition probabilities, radiative lifetimes, branching ratios, and cross-sections. It can also give us quantitative information on the non-radiative de-excitation process and intrinsic quantum efficiency if coupled with time-resolved luminescence measurements [38]. The main difficulty in applying the Judd-Ofelt theory is estimating the intensity parameters, Ω_λ, which is usually performed by fitting the intensities in the absorption spectrum to theoretical relations [39].

Europium is a unique ion among lanthanides as it has pure magnetic dipole transitions [40]. Magnetic dipole transitions, unaffected by the host matrix, can be used for calibrating the emission spectrum [41]. Thus, in Eu^{3+} doped materials only a single emission spectrum is sufficient for Judd-Ofelt parametrization, by using the equation [38]:

$$\Omega_\lambda = \frac{D_1}{e^2 U^\lambda} \left(\frac{\overline{\lambda}_\lambda}{\overline{\lambda}_1}\right)^3 \frac{9n_1^3}{n_\lambda(n_\lambda^2 + 2)^2} \frac{I_\lambda}{I_1}, \lambda = 2, 4, 6 \tag{3}$$

where e is the elementary charge, D_1 is the magnetic dipole strength, U^λ are the tabulated values of the squared reduced matrix elements, and n is the refractive index.

No refractive index values have been reported for Sr_2GdF_7. However, the refractive indices of SrF_2 and GdF_3 are well-established and documented in the literature [42–44]. The refractive index of Sr_2GdF_7 was approximately estimated by taking a weighted average of the refractive indices of SrF_2 and GdF_3, based on their relative contribution, from the dispersion relations given in the literature (see Fig. 4):

$$n_{avg}(Sr_2GdF_7) \approx \frac{2n(SrF_2) + n(GdF_3)}{3} \tag{4}$$

Transition $^5D_0 \rightarrow {}^7F_1$ is denoted with 1 in the subscript, while induced electric-dipole emissions $^5D_0 \rightarrow {}^7F_{\lambda=2,4,6}$ are denoted with λ=2,4,6 in the subscript. $I_{1,\lambda}$ are the integrated intensities of corresponding emissions.

The asymmetry ratio, a quantitative measure that shows the degree of deviation from the ideal site symmetry of Eu^{3+} ion in the host matrix, given by the ratio of integrated intensities of $^5D_0 \rightarrow {}^7F_2$ to $^5D_0 \rightarrow {}^7F_1$ emission, is directly proportional to the Ω_2 parameter [45]:
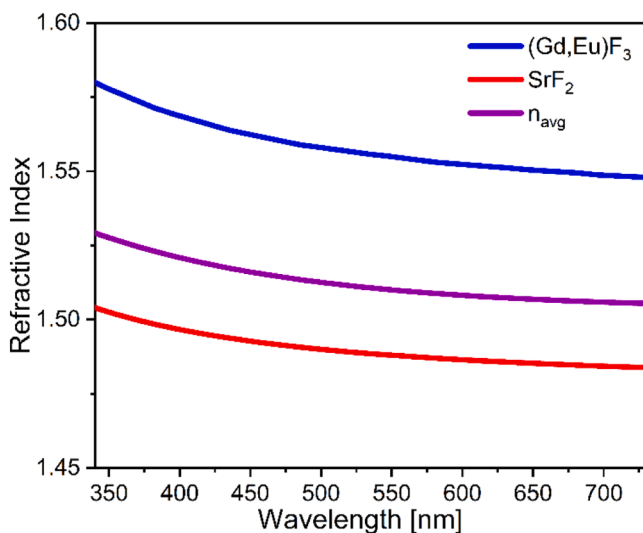

Fig. 4. Refractive index of GdF_3 and SrF_2 and approximative estimation of refractive index of Sr_2GdF_7.

$$R = \frac{I_2}{I_1} \propto \Omega_2 \tag{5}$$

The $^5D_0 \rightarrow {}^7F_6$ emission is of very low intensity and usually lies beyond the sensitive spectral range of most detectors. Thus, this part is most frequently neglected in the Judd-Ofelt analysis, which can lead to errors in estimates of derivative radiative quantities. In the recently published method, this Judd-Ofelt parameter can be accurately estimated from the excitation spectrum by [46]:

$$\Omega_6 = 0.459 \frac{n_6 n_1}{(n_6^2 + 2)^2} \frac{\overline{\lambda}_6}{\overline{\lambda}_1} \frac{\Gamma_6}{\Gamma_1} \bullet 10^{-20} cm^2, \tag{6}$$

where Γ are the integrated intensities of peaks in the excitation spectrum. Here 6 abbreviates $^7F_0 \rightarrow {}^5L_6$ and 1 in the subscript stands for $^7F_0 \rightarrow {}^5D_1$ transition.

From the Judd-Ofelt intensity parameters, the radiative transition probabilities for induced electric dipole transitions can be calculated by [37]:

$$A_\lambda = \frac{64\pi^4}{3h} \frac{10^7}{\overline{\lambda}_\lambda^3} \frac{n_\lambda(n_\lambda^2 + 2)^2}{9} e^2 \Omega_\lambda U^\lambda \tag{7}$$

and for magnetic dipole transition by:

$$A_1 = \frac{64\pi^4}{3h} \frac{10^7}{\overline{\lambda}_1^3} n_1^3. \tag{8}$$

The total radiative transition probability, or the rate of spontaneous emission, is then equal to the inverse of the radiative lifetime:

$$A_R = \sum_{i=1,2,4,6} A_i = \frac{1}{\tau_R} \tag{9}$$

Radiative transition probabilities provide estimates of emission branching ratios by:

$$\beta_{\lambda,1} = \frac{A_{\lambda,1}}{A_R} \tag{10}$$

De-excitation rates, A_{obs}, are experimentally measured as the inverse of the observable emission lifetime, which then enables the calculation of the non-radiative rates:

$$A_{NR} = A_{obs} - A_R = \frac{1}{\tau_{obs}} - A_R \tag{11}$$

Radiative transition probabilities enable the calculation of the emission cross-sections, given by the equation [47]:

$$\sigma_\lambda(\lambda_p) = \frac{\lambda_{max}^4}{8\pi c n_\lambda^2} \frac{maxI_\lambda}{I_\lambda} A_\lambda \tag{12}$$

where c is the speed of light, and λ_{max} is the position of the peak maximum.

The Judd-Ofelt intensity parameters of SGF with various Eu^{3+} concentrations are given in Table 3, together with estimated derived quantities: transition probabilities, branching ratios, cross-sections, and lifetimes. All the quantities for transitions $^5D_0 \rightarrow {}^7F_{1,2,4}$ are estimated by JOES software [47], while quantities for $^5D_0 \rightarrow {}^7F_6$ emission are calculated by JOEX software [46]. Due to the lower emission intensity in the spectra, the analysis for the sample with 5 % Eu^{3+} content has the largest error. Ω_2 parameter, as the measure of covalency and distortion of symmetry is largest for the samples with 60 % and 80 % of Eu^{3+}. A similar trend is observed with the Ω_4 parameter. Parameter Ω_6, associated with the rigidity of the matrix, decreases uniformly with an increase in Eu^{3+} concentration. The radiative transition probabilities confirm that the emission with the largest photon flux is to the $^7F_4$ level. The observable lifetime (τ_{obs}) decreases with increasing Eu^{3+} concentration due to changes in the local environment that influence radiative

Table 3
Judd-Ofelt parameters for SGF:Eu^{3+}.

[Eu] (%)	5	10	40	60	80	100
$\Omega_2 \cdot 10^{20}$ (cm^2)	0.41	0.99	0.98	1.17	1.17	1.08
$\Omega_4 \cdot 10^{20}$ (cm^2)	3.08	4.19	4.63	4.78	4.79	4.30
$\Omega_6 \cdot 10^{20}$ (cm^2)	1.91	1.38	1.10	0.88	0.86	0.85
A_1 (s^{-1})	23.0	23.0	23.0	23.0	23.0	23.0
A_2 (s^{-1})	6.3	14.2	14.0	16.8	16.9	15.5
A_4 (s^{-1})	22.6	30.4	33.6	34.7	34.8	31.2
A_6 (s^{-1})	1.1	0.8	0.6	0.5	0.5	0.5
β_1 (%)	44	34	32	31	31	33
β_2 (%)	12	21	20	22	22	22
β_4 (%)	43	44	47	46	46	44
β_6 (%)	2	1	1	1	1	1
$\sigma_1 \cdot 10^{22}$ (cm^2)	2.47	1.78	1.67	1.61	1.58	1.66
$\sigma_2 \cdot 10^{22}$ (cm^2)	0.74	0.74	0.74	0.84	0.84	0.79
$\sigma_4 \cdot 10^{22}$ (cm^2)	6.21	4.91	5.55	5.25	5.28	4.91
τ_{obs} (ms)	12.0	11.7	11.2	10.6	9.3	6.9
A_{obs} (s^{-1})	83.2	85.4	89.2	95.4	107.9	144.3
A_R (s^{-1})	52.9	68.3	71.3	75.0	75.1	70.1
A_{NR} (s^{-1})	30.3	17.1	17.9	20.4	32.7	74.1
τ_R (ms)	18.9	14.6	14.0	13.3	13.3	14.3
QE (%)	7.1	16.8	22.2	35.0	60.4	58.1

properties. However, the primary factor is the increasing probability of non-radiative relaxation (A_{NR}), predominantly caused by cross-relaxation between Eu^{3+} ions. The total radiative transition probability (A_R) rises up to a doping concentration of 80 %, leading to the lowest radiative lifetime (τ_R) at this point. This corresponds to the highest Judd-Ofelt parameters observed for this concentration. Despite this, as calculated from Eq. 10, the non-radiative rate continues to increase with concentration and eventually surpasses the radiative transition probability at the highest concentration. As a result, cross-relaxation at 100 % doping becomes substantial enough to significantly elevate the non-radiative rate, leading to a marked reduction in the observable lifetime (τ_{obs}).

3.2.2. Temperature-dependent photoluminescence measurements

To determine the temperature stability, temperature-dependent photoluminescence measurements in steady-state and time- domains were recorded in the 25–200 °C temperature range on dried samples in powder form. Fig. 5a shows the white color of powders under daylight and the red appearance under UV light, which becomes more intense as Eu^{3+} concentration increases. Fig. 5b shows the lifetime, while Fig. 5c shows the emission intensity as a function of temperature for two representative samples, SGF_5Eu (with the lowest Eu^{3+} content in the series) and the SGF_80Eu sample, with the highest emission intensity. For both samples, lifetime values show high-temperature stability in the temperature range relevant for LEDs, while emission intensity shows a slight decrease in the same range. It is important to note that, depending on the manufacturer, 100°C is usually considered the maximal operating temperature of LEDs [48,49], while temperature stability up to 150°C is frequently given in the literature [15,50]. For SGF_80Eu, the sample with the highest emission intensity, the lifetime, and the emission intensity at 100°C remain at 95 % and 83 % of their initial values at room temperature, respectively. It is generally acknowledged that Eu^{3+}'s 4f electrons are effectively shielded, and the primary de-excitation pathways of the $^5D_0$ level occur through cross-over with the charge transfer band or multiphonon relaxation [51]. In fluoride matrices, the charge transfer bands are energetically far from the $^5D_0$ level, and these matrices are characterized by low phonon energies, resulting in a lower probability of temperature-induced de-excitation in SGF:Eu^{3+}. However, a marked decline in stability is observed for SGF_80Eu beyond 100°C, in contrast to the consistently stable SGF_5 across all temperatures. This suggests that cross-relaxation effects become more prominent with increasing temperature at higher Eu^{3+} concentrations. In addition to our findings, Table 4 includes previously reported excitation and emission wavelength, QE values, and temperature stability for far-red-emitting phosphors produced for indoor plant growth LEDs. Findings shown in Table 4 are mainly based on Mn^{4+}-doped phosphors, while the literature reports on the Eu^{3+}-activated oxide phosphors as prospective candidates for horticulture LEDs are scarce.
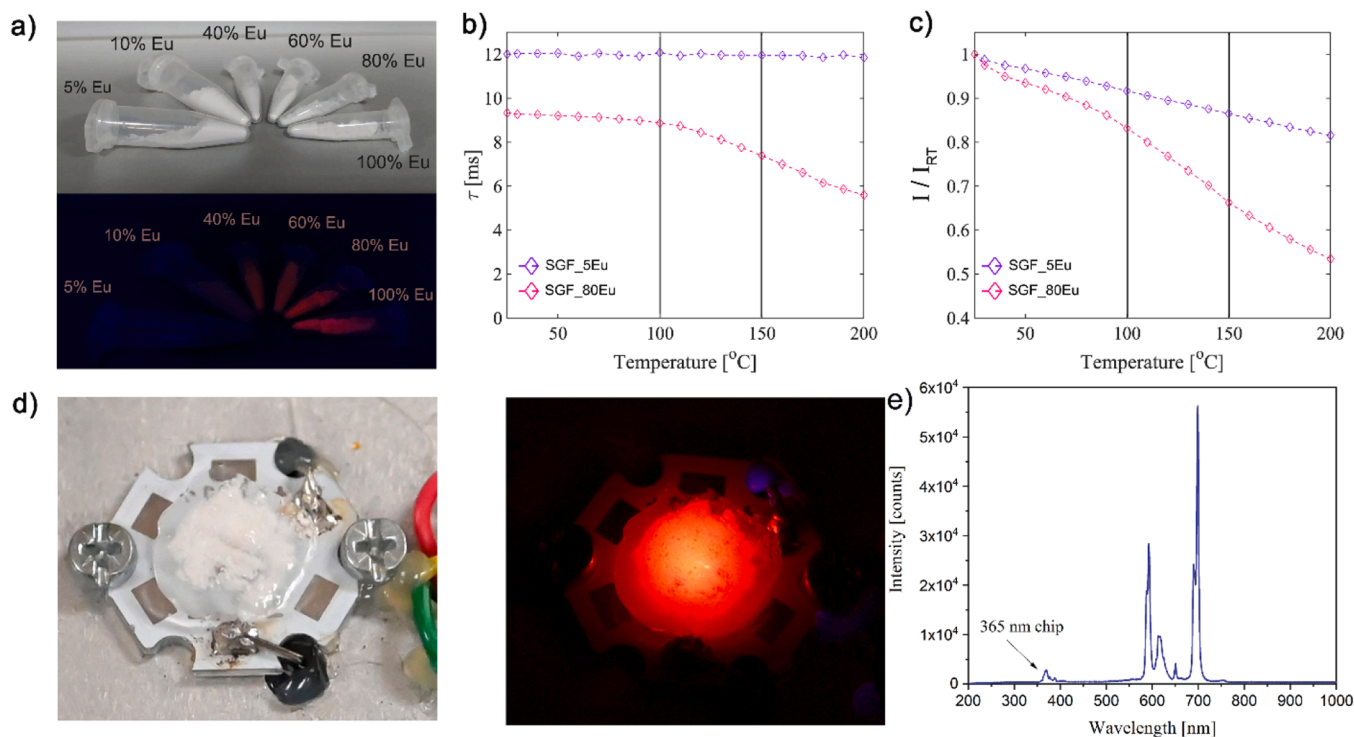
Fig. 5. a) Appearance of nanopowders under daylight and near UV light. Temperature-dependence of b) lifetime and c) emission intensity for the whole set of nanopowders. d) A fabricated LED device comprising a semiconductor chip and SGF_80Eu nanopowders displays a red light when the electrical power supply is on. e) PL spectrum of the fabricated LED.

Table 4
QE values and temperature stability for some previously reported far-red phosphors.

Far-red-emitting phosphors	λ_{ex} (nm), λ_{em} (nm)	QE (%)	Thermal stability (I_{373K}/I_{303K})	Thermal stability (I_{423K}/I_{303K})	Ref.
SGF_80Eu	394, 698	60.4	83 %	66 %	This work
Li_2MgZrO_4:Mn^{4+}	335, 675	32.3	75 %	58 %	[52]
Ca_2LuSbO_6:Mn^{4+}	345, 683	39.1	66 %	48 %	[53]
La_2ZnTiO_6:Mn^{4+}	342, 708	-	81 %	64 %	[54]
$CaYAlO_4$:Mn^{4+}	370, 710	26	50 %	70 %	[55]
$NaLaMgWO_6$:Mn^{4+}	342, 700	60	-	57 %	[56]
$Ca_9MY_{0.667}(PO_4)_7$:Eu^{3+} (M = Li, Na)	394, 700	-	-	-	[57]
Lu_2GeO_5:Bi^{3+},Eu^{3+}	313,710	43	70 %	51 %	[58]

Finally, we mixed the powder sample of the highest emission intensity, SGF_80Eu, with a ceramic binder and placed it on top of a 365 nm near-UV LED chip to demonstrate the application potential of these materials in LEDs. Photographs of the fabricated LED device, presented in Fig. 5d, display a red light when the power supply is on. In addition, Fig. 5e shows the PL spectrum of the fabricated LED device with CIE coordinates (0.5759, 0.3893) and low correlated color temperature (CCT = 1534 K).

4. Conclusion

We have prepared a series of Eu^{3+}-doped Sr_2GdF_7 nanoparticles and synthesized them in both colloid and powder forms using the hydrothermal method. We have analyzed structural, morphological, and photoluminescent properties in detail and demonstrated:

(i) The cubic structure of SGF was confirmed by Rietveld refinement.
(ii) Very high light output, owing to the concentration quenching not being reached even at 80 % replacement of Gd^{3+} by Eu^{3+} ions, and the consequent presence of large numbers of active emission centers;
(iii) PL spectra show Eu^{3+} red emission bands ($^5D_0\rightarrow^7F_1$ and $^5D_0\rightarrow^7F_2$) match the red-adsorbing phytochrome photoreceptors, P_R
(iv) The strongest $^5D_0\rightarrow^7F_4$ emission at ~ 700 nm matches the PAR radiation of phytochrome photoreceptors P_{FR}, making these materials suitable for the construction of indoor plant growth LEDs.
(v) The lifetime and emission intensity of the representative sample SGF:80Eu at 100°C remain 95 % and 83 % of their initial values at room temperature, respectively.
(vi) PL lifetime and QE of SGF:80 %Eu^{3+} phosphor at room temperature are ~ 9.3 ms and 60.4 %, respectively.

These findings indicate that a variety of applications, particularly in sustainable agriculture, could benefit from the highly efficient red-emitting colloidal and powder nanophosphors. We will further investigate the system's optical and chemical stability in humid agricultural conditions.

CRediT authorship contribution statement

Miroslav Dramićanin: Writing – review & editing, Methodology, Conceptualization. **Ivana Evans:** Writing – review & editing, Visualization, Formal analysis. **Željka Antić:** Writing – original draft, Investigation, Formal analysis. **Abdullah Alodhayb:** Visualization, Data curation. **Zoran Ristić:** Visualization, Data curation. **Mina Medić:** Visualization, Data curation. **Bojana Milićević:** Writing – original draft, Visualization, Investigation, Formal analysis, Data curation. **Aleksandar Ćirić:** Visualization, Formal analysis, Data curation.

Declaration of Competing Interest

The authors declare that they have no known competing financial interests or personal relationships that could have appeared to influence the work reported in this paper.

Data Availability

Data will be made available on request.

References

[1] M.D. Dramićanin, Trends in luminescence thermometry, J. Appl. Phys. 128 (2020), https://doi.org/10.1063/5.0014825.
[2] N. Jaroch, J. Czajka, A. Szczeszak, Luminescent materials with dual-mode excitation and tunable emission color for anti-counterfeiting applications, Sci. Rep. 13 (2023) 10773, https://doi.org/10.1038/s41598-023-37608-w.
[3] J. Shen, L.-D. Sun, C.-H. Yan, Luminescent rare earth nanomaterials for bioprobe applications, Dalt. Trans. (2008) 5687, https://doi.org/10.1039/b805306e.
[4] M. Ye, C. Yang, A. Wang, G. Chen, D. Yuan, W. Zhou, Advancing red-emitting fluoride phosphors for highly stable white light-emitting diodes: crystal reconstruction and covalence enhancement strategy, Inorg. Chem. 62 (2023) 12130–12137, https://doi.org/10.1021/acs.inorgchem.3c01709.
[5] J. Zhou, Y. Wang, Y. Chen, Y. Zhou, B. Milićević, L. Zhou, J. Yan, J. Shi, R. Liu, M. Wu, Single-crystal red phosphors and their core–shell structure for improved water-resistance for laser diodes applications, Angew. Chem. Int. Ed. 60 (2021) 3940–3945, https://doi.org/10.1002/anie.202011022.
[6] N.U. Rahman, W.U. Khan, S. Khan, X. Chen, J. Khan, J. Zhao, Z. Yang, M. Wu, Z. Chi, A promising europium-based down conversion material: organic–inorganic perovskite solar cells with high photovoltaic performance and UV-light stability, J. Mater. Chem. A 7 (2019) 6467–6474, https://doi.org/10.1039/C9TA00551J.
[7] S. Fang, T. Lang, T. Cai, T. Han, Light keys open locks of plant photoresponses: a review of phosphors for plant cultivation LEDs, J. Alloy. Compd. 902 (2022) 163825, https://doi.org/10.1016/j.jallcom.2022.163825.
[8] C.R. Ronda, Recent achievements in research on phosphors for lamps and displays, J. Lumin 72–74 (1997) 49–54, https://doi.org/10.1016/S0022-2313(96)00374-2.
[9] B.-H. Jun, Advanced optical materials: from materials to applications, Int. J. Mol. Sci. 24 (2023) 15790, https://doi.org/10.3390/ijms242115790.
[10] H.-M. Kim, J. Kim, J. An, S. Bock, X.-H. Pham, K.-H. Huynh, Y. Choi, E. Hahm, H. Song, J.-W. Kim, W.-Y. Rho, D.H. Jeong, H.-Y. Lee, S. Lee, B.-H. Jun, Au–Ag assembled on silica nanoprobes for visual semiquantitative detection of prostate-specific antigen, J. Nanobiotechnol. 19 (2021) 73, https://doi.org/10.1186/s12951-021-00817-4.
[11] H.-M. Kim, C. Oh, J. An, S. Baek, S. Bock, J. Kim, H.-S. Jung, H. Song, J.-W. Kim, A. Jo, D.-E. Kim, W.-Y. Rho, J.-Y. Jang, G.J. Cheon, H.-J. Im, B.-H. Jun, Multi-quantum dots-embedded silica-encapsulated nanoparticle-based lateral flow assay for highly sensitive exosome detection, Nanomaterials 11 (2021) 768, https://doi.org/10.3390/nano11030768.
[12] X.-H. Pham, E. Hahm, E. Kang, Y.N. Ha, S.H. Lee, W.-Y. Rho, Y.-S. Lee, D.H. Jeong, B.-H. Jun, Gold-silver bimetallic nanoparticles with a Raman labeling chemical assembled on silica nanoparticles as an internal-standard-containing nanoprobe, J. Alloy. Compd. 779 (2019) 360–366, https://doi.org/10.1016/j.jallcom.2018.11.270.
[13] S.H. Lee, B.-H. Jun, Advances in dynamic microphysiological organ-on-a-chip: design principle and its biomedical application, J. Ind. Eng. Chem. 71 (2019) 65–77, https://doi.org/10.1016/j.jiec.2018.11.041.
[14] S. Zhen, B. Bugbee, Far-red photons have equivalent efficiency to traditional photosynthetic photons: Implications for redefining photosynthetically active radiation, Plant. Cell Environ. 43 (2020) 1259–1272, https://doi.org/10.1111/pce.13730.
[15] C. Yang, W. Liu, Q. You, X. Zhao, S. Liu, L. Xue, J. Sun, X. Jiang, Recent advances in light-conversion phosphors for plant growth and strategies for the modulation of photoluminescence properties, Nanomaterials 13 (2023) 1715, https://doi.org/10.3390/nano13111715.
[16] B. Milićević, J. Periša, Z. Ristić, K. Milenković, Ž. Antić, K. Smits, M. Kemere, K. Vitols, A. Sarakovskis, M. Dramićanin, Hydrothermal synthesis and properties of

Yb^{3+}/Tm^{3+} doped Sr$_2$LaF$_7$ upconversion nanoparticles, Nanomaterials 13 (2022) 30, https://doi.org/10.3390/nano13010030.

[17] H.M. Rietveld, A profile refinement method for nuclear and magnetic structures, J. Appl. Crystallogr. 2 (1969) 65–71, https://doi.org/10.1107/S0021889869006558.

[18] A.A. Coelho, J. Evans, I. Evans, A. Kern, S. Parsons, The T$_{OPAS}$ symbolic computation system, Powder Diffr. 26 (2011) S22–S25, https://doi.org/10.1154/1.3661087.

[19] R.D. Shannon, Revised effective ionic radii and systematic studies of interatomic distances in halides and chalcogenides, Acta Crystallogr. Sect. A 32 (1976) 751–767, https://doi.org/10.1107/S0567739476001551.

[20] W. Chen, J. Cao, F. Hu, R. Wei, L. Chen, H. Guo, Sr$_2$GdF$_7$:Tm^{3+}/Yb^{3+} glass ceramic: a highly sensitive optical thermometer based on FIR technique, J. Alloy. Compd. 735 (2018) 2544–2550, https://doi.org/10.1016/j.jallcom.2017.11.201.

[21] L. Teng, W. Zhang, W. Chen, J. Cao, X. Sun, H. Guo, Highly efficient luminescence in bulk transparent Sr$_2$GdF$_7$:Tb^{3+} glass ceramic for potential X-ray detection, Ceram. Int. 46 (2020) 10718–10722, https://doi.org/10.1016/j.ceramint.2020.01.079.

[22] Z. Xia, P. Du, L. Liao, Facile hydrothermal synthesis and upconversion luminescence of tetragonal Sr$_2$LnF$_7$:Yb^{3+}/Er^{3+} (Ln = Y, Gd) nanocrystals, Phys. Status Solidi 210 (2013) 1734–1737, https://doi.org/10.1002/pssa.201329114.

[23] C. Chen, J. Liu, Y. Chen, C. Li, X. Liu, H. Huang, C. Liang, Y. Lou, Z. Shi, S. Feng, Sub-10 nm Sr$_2$LuF$_7$:Yb/Er@Sr$_2$GdF$_7$@SrF$_2$ up-conversion nanocrystals for up-conversion luminescence–magnetic resonance–computed tomography trimodal bioimaging, ACS Appl. Mater. Interfaces 9 (2017) 5748–5756, https://doi.org/10.1021/acsami.6b14007.

[24] F. Hu, J. Zhang, O. Giraldo, W. Song, R. Wei, M. Yin, H. Guo, Spectral conversion from green to red in Yb^{3+}/Ho^{3+}:Sr$_2$GdF$_7$ glass ceramics via Ce^{3+} doping, J. Lumin. 201 (2018) 493–499, https://doi.org/10.1016/j.jlumin.2018.05.007.

[25] L. Xiang, G. Ren, Y. Mao, J. He, R. Su, Controllable synthesis and upconversion emission of ultrasmall lanthanide-doped Sr$_2$GdF$_7$ nanoparticles, Opt. Mater. (Amst.) 49 (2015) 6–14, https://doi.org/10.1016/j.optmat.2015.08.014.

[26] S. Sarkar, L. Graña-Suárez, W. Verboom, V. Mahalingam, J. Huskens, A luminescent nanocrystal marker for the selective and ultrasensitive detection of explosives, ChemNanoMat 2 (2016) 805–809, https://doi.org/10.1002/cnma.201600184.

[27] T. Grzyb, D. Przybylska, Formation mechanism, structural, and upconversion properties of alkaline rare-earth fluoride nanocrystals doped with Yb^{3+}/Er^{3+} ions, Inorg. Chem. 57 (2018) 6410–6420, https://doi.org/10.1021/acs.inorgchem.8b00484.

[28] N.I. Sorokin, D.N. Karimov, E.A. Sul'yanova, B.P. Sobolev, Nanostructured crystals of fluorite phases Sr$_{1−x}$R$_x$F$_{2+x}$ and their ordering: 12. influence of structural ordering on the fluorine-ion conductivity of Sr0.667R0.333F2.333 Alloys (R = Tb or Tm) at their annealing, Crystallogr. Rep. 63 (2018) 121–126, https://doi.org/10.1134/S1063774518010182.

[29] J.L. Payne, M.G. Tucker, I.R. Evans, From fluorite to pyrochlore: characterisation of local and average structure of neodymium zirconate, Nd$_2$Zr$_2$O$_7$, J. Solid State Chem. 205 (2013) 29–34, https://doi.org/10.1016/j.jssc.2013.07.001.

[30] P. Dang, G. Li, X. Yun, Q. Zhang, D. Liu, H. Lian, M. Shang, J. Lin, Thermally stable and highly efficient red-emitting Eu^{3+}-doped Cs$_3$GdGe$_3$O$_9$ phosphors for WLEDs: non-concentration quenching and negative thermal expansion, Light Sci. Appl. 10 (2021) 29, https://doi.org/10.1038/s41377-021-00469-x.

[31] M. Dejneka, E. Snitzer, R.E. Riman, Blue, green and red fluorescence and energy transfer of Eu^{3+} in fluoride glasses, J. Lumin. 65 (1995) 227–245, https://doi.org/10.1016/0022-2313(95)00073-9.

[32] L. Xiang, X. Zhou, L. Li, F. Ling, Y. Li, J. Li, H. Yang, Comparative study on the anomalous intense ^{5}D$_0$→^{7}F$_4$ emission in Eu^{3+} doped Sr$_2$MNbO$_6$ (M=Ga, In, Gd) phosphors, J. Lumin. 267 (2024) 120370, https://doi.org/10.1016/j.jlumin.2023.120370.

[33] G. Blasse, Luminescence from the Eu^{3+} ion in D$_{4d}$ symmetry, Inorg. Chim. Acta 142 (1988) 153–154, https://doi.org/10.1016/S0020-1693(00)80674-X.

[34] R.A. Sá Ferreira, S.S. Nobre, C.M. Granadeiro, H.I.S. Nogueira, L.D. Carlos, O.L. Malta, A theoretical interpretation of the abnormal ^{5}D$_0$→^{7}F$_4$ intensity based on the Eu^{3+} local coordination in the Na$_9$[EuW$_{10}$O$_{36}$]·14H$_2$O polyoxometalate, J. Lumin. 121 (2006) 561–567, https://doi.org/10.1016/j.jlumin.2005.12.044.

[35] B.R. Judd, Optical absorption intensities of rare-Earth ions, Phys. Rev. 127 (1962) 750–761, https://doi.org/10.1103/PhysRev.127.750.

[36] G.S. Ofelt, Intensities of crystal spectra of rare-Earth ions, J. Chem. Phys. 37 (1962) 511–520, https://doi.org/10.1063/1.1701366.

[37] M.P. Hehlen, M.G. Brik, K.W. Krämer, 50th anniversary of the Judd–Ofelt theory: an experimentalist's view of the formalism and its application, J. Lumin. 136 (2013) 221–239, https://doi.org/10.1016/j.jlumin.2012.10.035.

[38] K. Binnemans, Interpretation of europium(III) spectra, Coord. Chem. Rev. 295 (2015) 1–45, https://doi.org/10.1016/j.ccr.2015.02.015.

[39] B.M. Walsh, Judd-Ofelt theory: principles and practices. Adv. Spectrosc. Lasers Sens., Springer Netherlands, Dordrecht, 2006, pp. 403–433, https://doi.org/10.1007/1-4020-4789-4_21.

[40] C.M. Dodson, R. Zia, Magnetic dipole and electric quadrupole transitions in the trivalent lanthanide series: Calculated emission rates and oscillator strengths, Phys. Rev. B 86 (2012) 125102, https://doi.org/10.1103/PhysRevB.86.125102.

[41] C. Görller-Walrand, L. Fluyt, A. Ceulemans, W.T. Carnall, Magnetic dipole transitions as standards for Judd–Ofelt parametrization in lanthanide spectra, J. Chem. Phys. 95 (1991) 3099–3106, https://doi.org/10.1063/1.460867.

[42] D. Franta, J. Vohánka, J. Dvořák, P. Franta, I. Ohlídal, P. Klapetek, J. Březina, D. Škoda, Optical characterization of gadolinium fluoride films using universal dispersion model, Coatings 13 (2023) 218, https://doi.org/10.3390/coatings13020218.

[43] R. Thielsch, J. Heber, H. Uhlig, N. Kaiser, Optical, structural, and mechanical properties of gadolinium tri-fluoride thin films grown on amorphous substrates, in: C. Amra, N. Kaiser, H.A. Macleod (Eds.), 2005: p. 59630O. https://doi.org/10.1117/12.625096.

[44] L.R. Marcos, J.I. Larruquert, J.A. Aznárez, M. Fernández-Perea, R. Soufli, J.A. Méndez, S.L. Baker, E.M. Gullikson, Optical constants of SrF$_2$ thin films in the 25–780-eV spectral range, J. Appl. Phys. 113 (2013), https://doi.org/10.1063/1.4800099.

[45] P.A. Tanner, Some misconceptions concerning the electronic spectra of tri-positive europium and cerium, Chem. Soc. Rev. 42 (2013) 5090, https://doi.org/10.1039/c3cs60033e.

[46] A. Ćirić, M. Marciniak, M.D. Dramićanin, Self-referenced method for the Judd–Ofelt parametrisation of the Eu^{3+} excitation spectrum, Sci. Rep. 12 (2022) 563, https://doi.org/10.1038/s41598-021-04651-4.

[47] A. Ćirić, S. Stojadinović, M. Sekulić, M.D. Dramićanin, JOES: an application software for Judd-Ofelt analysis from Eu^{3+} emission spectra, J. Lumin. 205 (2019) 351–356, https://doi.org/10.1016/j.jlumin.2018.09.048.

[48] OSRAM, LB QH9G Chip LED 0402 Datasheet, (n.d.). https://look.ams-osram.com/m/3184c82bafe7f3ef/original/LB-QH9G.pdf (accessed March 20, 2024).

[49] XLamp, XLAMP® WHITE LEDs, (n.d.). https://downloads.cree-led.com/files/fs/XLamp-Discrete-Directional-Feature-Sheet.pdf (accessed March 20, 2024).

[50] Y. Liu, J. Zhang, C. Zhang, J. Xu, G. Liu, J. Jiang, H. Jiang, Ba$_9$Lu$_2$Si$_6$O$_{24}$:Ce^{3+}: an efficient green phosphor with high thermal and radiation stability for solid-state lighting, Adv. Opt. Mater. 3 (2015) 1096–1101, https://doi.org/10.1002/adom.201500078.

[51] A. Ćirić, M.D. Dramićanin, LumTHools - Software for fitting the temperature dependence of luminescence emission intensity, lifetime, bandshift, and bandwidth and luminescence thermometry and review of the theoretical models, J. Lumin. 252 (2022) 119413, https://doi.org/10.1016/j.jlumin.2022.119413.

[52] R. Cao, Z. Shi, G. Quan, T. Chen, S. Guo, Z. Hu, P. Liu, Preparation and luminescence properties of Li$_2$MgZrO$_4$:Mn^{4+} red phosphor for plant growth, J. Lumin. 188 (2017) 577–581, https://doi.org/10.1016/j.jlumin.2017.05.002.

[53] J. Liang, B. Devakumar, L. Sun, S. Wang, Q. Sun, H. Guo, X. Huang, Deep-red-emitting Ca$_2$LuSbO$_6$:Mn^{4+} phosphors for plant growth LEDs: Synthesis, crystal structure, and photoluminescence properties, J. Alloy. Compd. 804 (2019) 521–526, https://doi.org/10.1016/j.jallcom.2019.06.312.

[54] Z. Yang, L. Yang, C. Ji, D. Xu, C. Zhang, H. Bu, X. Tan, X. Yun, J. Sun, Studies on luminescence properties of double perovskite deep red phosphor La$_2$ZnTiO$_6$:Mn^{4+} for indoor plant growth LED applications, J. Alloy. Compd. 802 (2019) 628–635, https://doi.org/10.1016/j.jallcom.2019.06.199.

[55] Y. Chen, M. Wang, J. Wang, M. Wu, C. Wang, A high color purity red emitting phosphor CaYAlO$_4$:Mn^{4+} for LEDs, J. Solid State Light. 1 (2014) 15, https://doi.org/10.1186/s40539-014-0015-4.

[56] X. Huang, J. Liang, B. Li, L. Sun, J. Lin, High-efficiency and thermally stable far-red-emitting NaLaMgWO$_6$:Mn^{4+} phosphorsfor indoor plant growth light-emitting diodes, Opt. Lett. 43 (2018) 3305, https://doi.org/10.1364/OL.43.003305.

[57] S. Wang, Y. Han, L. Shi, Y. Tong, Q. Zhao, J. Zhang, Z. Mao, Z. Mu, Z. Zhang, S. Niu, A new strategy to the phosphors for plant growth LEDs: Far red emission from the Ca$_9$MY$_{0.667}$(PO$_4$)$_7$ (M = Li, Na):Eu^{3+} phosphors due to the Eu^{3+}: ^{5}D$_0$ → ^{7}F$_4$ transition, J. Lumin 225 (2020) 117404, https://doi.org/10.1016/j.jlumin.2020.117404.

[58] L. Sun, B. Devakumar, J. Liang, S. Wang, Q. Sun, X. Huang, Novel high-efficiency violet-red dual-emitting Lu$_2$GeO$_5$:Bi^{3+}, Eu^{3+} phosphors for indoor plant growth lighting, J. Lumin. 214 (2019) 116544, https://doi.org/10.1016/j.jlumin.2019.116544.